Metabolite concentrations, fluxes and free energies imply efficient enzyme usage

Junyoung O Park[1,2], Sara A Rubin[3], Yi-Fan Xu[1,3,5], Daniel Amador-Noguez[1,5], Jing Fan[1,3], Tomer Shlomi[4] & Joshua D Rabinowitz[1,3]*

In metabolism, available free energy is limited and must be divided across pathway steps to maintain a negative ΔG throughout. For each reaction, ΔG is log proportional both to a concentration ratio (reaction quotient to equilibrium constant) and to a flux ratio (backward to forward flux). Here we use isotope labeling to measure absolute metabolite concentrations and fluxes in *Escherichia coli*, yeast and a mammalian cell line. We then integrate this information to obtain a unified set of concentrations and ΔG for each organism. In glycolysis, we find that free energy is partitioned so as to mitigate unproductive backward fluxes associated with ΔG near zero. Across metabolism, we observe that absolute metabolite concentrations and ΔG are substantially conserved and that most substrate (but not inhibitor) concentrations exceed the associated enzyme binding site dissociation constant (K_m or K_i). The observed conservation of metabolite concentrations is consistent with an evolutionary drive to utilize enzymes efficiently given thermodynamic and osmotic constraints.

Absolute metabolite concentrations determine enzyme binding site occupancies[1] and the thermodynamics of metabolic reactions[2]. Accordingly, knowledge of absolute metabolite concentrations is valuable for dynamic modeling of metabolism[3,4]. Such knowledge is also useful for conducting *in vitro* enzyme assays under physiologically relevant conditions[5,6], predicting whether antimetabolites will outcompete with endogenous metabolites for relevant enzyme binding sites[7] and engineering enzymes that selectively bind desired substrates in the complex cellular environment[8].

A variety of methods exist for measuring cellular metabolite concentrations, with LC/MS enabling measurements of many metabolites with sensitivity and specificity[9,10]. A deficiency of LC/MS is that absolute signal intensity depends on ionization efficiency and therefore does not reliably reflect absolute concentrations. This limitation can be overcome by comparing the signal of endogenous metabolites to isotopically labeled standards, whose addition before extraction also accounts for losses in sample handling[11]. Because isotopically labeled standards of many metabolites are not commercially available, it is often more convenient to feed isotopically labeled substrates to cells and compare labeled intracellular metabolites to unlabeled standards[12]. Through this approach, we have previously measured the absolute concentrations of 103 metabolites in *E. coli*[1]. The concentrations of these metabolites are typically higher than the associated Michaelis constants (K_m) of the enzymes consuming them, suggesting that most active sites in *E. coli* are occupied.

Using these absolute concentrations, the thermodynamics (Gibbs free energy of reaction, ΔG) of metabolic reactions have also been assessed on the basis of the fundamental equation, where $\Delta G^{o\prime}$ is ΔG at standard biochemical conditions, Q is the reaction quotient (the ratio of the product to reactant activities), R is the gas constant, T is the temperature in Kelvin and K_{eq} is the equilibrium constant (the ratio of product to reactant activities at equilibrium) at standard biochemical conditions:

$$\Delta G = \Delta G^{o\prime} + RT \ln Q = RT \ln (Q/K_{eq}) \qquad (1)$$

For simplicity, Q is typically calculated on the basis of concentrations, not activities, using $\Delta G^{o\prime}$ determined at cellular ionic strength and divalent cation concentrations.

The ΔG has been applied in metabolic analysis to eliminate flux loops that violate the second law of thermodynamics[13,14] and to constrain the directions of cellular metabolic reactions[15]. In addition, it determines the fraction of flux through metabolic reactions that is in the forward direction and thus productive and thereby relates to the efficiency of enzyme utilization[16]. Thermodynamic analysis also can provide regulatory insights, with enzymes operating far from equilibrium being more effective targets for regulating pathway flux[17].

Here we explore the potential to infer cellular reaction free energies on the basis of relative forward-to-backward flux. Specifically, where J^+ and J^- are forward and backward fluxes[18–20]:

$$\Delta G = -RT \ln (J^+/J^-) \qquad (2)$$

We validated that the relative forward and backward flux ratios through reversible reactions like triose phosphate isomerase can be measured using isotope tracers. Moreover, we recognized that the resulting ΔG measurements can be used to evaluate the metabolite concentrations. For example, given direct measurements of the reversibility and all but one of the substrates or products of a reaction, the missing concentration can be determined by combining equations (1) and (2). More generally, concentrations, fluxes and thermodynamics are all interrelated, and we aimed to obtain coherent values of each.

This integrative analysis was conducted in *E. coli*, yeast, and a cultured mammalian cell line. The mammalian cell line (iBMK) was derived by immortalization of baby mouse kidney cells[21]. Each cell type was grown in nutrient-rich conditions including high glucose. Under such media conditions, we observed that absolute metabolite concentrations are substantially conserved across these highly divergent cell types, arguing for a common set of constraints on their metabolomes. We propose that the three

[1]Lewis-Sigler Institute for Integrative Genomics, Princeton University, Princeton, New Jersey, USA. [2]Department of Chemical and Biological Engineering, Princeton University, Princeton, New Jersey, USA. [3]Department of Chemistry, Princeton University, Princeton, New Jersey, USA. [4]Department of Computer Science, Technion–Israel Institute of Technology, Haifa, Israel. [5]Present addresses: DuPont Industrial Biosciences, Experimental Station, Wilmington, Delaware, USA (Y.-F.X.),Department of Bacteriology and Great Lake Bioenergy Research Center, University of Wisconsin–Madison, Madison, Wisconsin, USA (D.A.-N.). *e-mail: joshr@princeton.edu

most important constraints are thermodynamics, osmotics and efficient enzyme utilization.

RESULTS

Isotope tracers reveal reaction reversibility and thus ΔG

To lay the groundwork for integrative analysis of metabolite concentrations, fluxes and free energies (**Fig. 1a**), we initially set out to validate the ability to measure the reversibility of a single glycolytic reaction catalyzed by triose phosphate isomerase (TPI) using isotope tracers. TPI converts dihydroxyacetone phosphate (DHAP) into glyceraldehyde-3-phosphate (GAP). To determine TPI reversibility, we needed a tracer that differentially labels DHAP and GAP. We selected $[1,2-^{13}C_2]$glucose, which yields $[1,2-^{13}C_2]$fructose-1,6-bisphosphate, the parent molecule of DHAP and GAP. DHAP is formed from carbons 1–3, and GAP is formed from carbons 4–6 (**Fig. 1b**). Thus, in the absence of backwards flux through TPI, all of the DHAP molecules would be labeled (M+2), with reverse flux through TPI resulting in the appearance of unlabeled DHAP.

To verify that we can measure different extents of reversibility, we knocked out the chromosomal TPI in *E. coli* and introduced an inducible TPI plasmid. At low inducer levels, DHAP was almost completely labeled, indicating nearly unidirectional forward flux (**Fig. 1c**). Increasing the inducer level resulted in unlabeled DHAP (up to a maximum value of 50% unlabeled), as expected for complete reversibility (**Fig. 1c**). The extent of DHAP labeling at pseudo-steady state can be converted into a ratio of forward-to-backward TPI flux on the basis of isotopomer balancing (Online Methods). Using equation (2), the forward-to-backward flux ratios yield ΔG_{TPI}. Because DHAP absolute concentration can be directly measured, we can determine the absolute concentration of GAP (which is less abundant and can be obscured by analytical interferences[22]) using equation (1).

Large-scale determination of net and exchange fluxes

The same conceptual approach that was applied to TPI can be expanded to cover a wide spectrum of central metabolic reactions. Analyzing the broader network advantageously accounts for all major sources and sinks of each metabolite but requires a diversity of tracers to quantify fluxes throughout central metabolism. Independent experiments feeding multiple different $[^{13}C]$glucose tracers and measuring pseudo-steady-state metabolite labeling

patterns by LC/MS were conducted in *E. coli*, yeast and the mammalian cell line iBMK. In addition, for the mammalian cells, tracer analysis was also conducted with $[U-^{13}C_5]$glutamine, another important carbon source for these cells. Labeling data are shown in **Supplementary Results**, **Supplementary Data Set 1**. Together with nutrient uptake and waste excretion data, the labeling data were sufficient to determine pseudo-steady-state net fluxes throughout central metabolism by isotopomer and flux balancing. Results of all of the tracer experiments were integrated into a single unified flux set for each organism (**Fig. 2a** and **Supplementary Table 1**).

Substantial differences in net fluxes were observed across the three organisms. The absolute glucose uptake rate, normalized to cell volume, was about 30-fold lower in the mammalian iBMK cells than in *E. coli* or yeast. Although the largest intracellular flux in each organism was glycolysis, they differed in their utilization of the pentose phosphate pathway and the tricarboxylic acid (TCA) cycle. Net flux through the oxidative pentose phosphate pathway was 20% of glucose uptake in *E. coli* but only 3% and 2% in yeast and mammalian iBMK cells, respectively. Flux of glucose-derived two-carbon units into the TCA cycle consumed 24% of pyruvate made in *E. coli* but only 13% in the mammalian iBMK cells and 2% in yeast, which had minimal α-ketoglutarate dehydrogenase flux, with malate dehydrogenase operating net in reverse. Malic enzyme flux was substantial in yeast and mammalian cells but not *E. coli*. Overall, fluxes were more similar in the two eukaryotic cell types than across the two microbes (**Fig. 2b**).

In addition to determining net fluxes, an in-house algorithm was developed to quantify forward-to-backward flux ratios and their confidence intervals and associated ΔG (Online Methods). The ability to obtain informative flux ratios depends on the backwards reaction producing a distinctive labeling pattern. The tracers employed enabled such direct measurement of forward-to-backward flux ratios for selected reactions in the pentose phosphate pathway, glycolysis, the TCA cycle and folate-mediated serine-glycine interconversion (**Fig. 3** and **Supplementary Table 2**).

Integrating metabolite concentrations and free energies

With an eye toward a better understanding of the overall thermodynamics of central carbon metabolism, we aimed to combine the flux-based free energy measurements from **Figure 3** with direct measurements of metabolite concentrations by LC/MS into a coherent
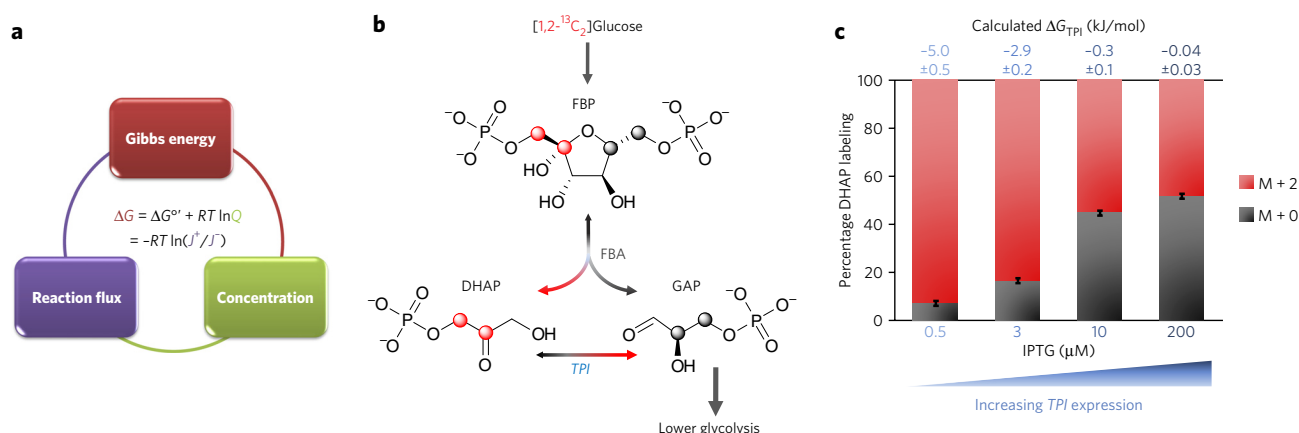

Figure 1 | Tracing forward-to-backward flux through TPI. (**a**) The free energy of cellular reactions is independently determined by (i) the reaction standard free energy adjusted for substrate and product concentrations and (ii) the ratio of forward-to-backward fluxes. The integration of experimental measurements of forward-to-backward reaction fluxes and of metabolite concentrations results in more coherent and precise determination of both concentrations and ΔG. (**b**) $[1,2-^{13}C_2]$glucose (red atom represents ^{13}C) yields $[1,2-^{13}C_2]$fructose-1,6-bisphosphate (FBP), the parent molecule of DHAP and GAP. FBP carbons 1–3 form DHAP. Thus, in the absence of backwards flux through TPI, all DHAP molecules would be labeled (M+2). Reverse flux through TPI results in the appearance of unlabeled DHAP. (**c**) To verify that we can measure different extents of reversibility, we knocked out in *E. coli* the chromosomal TPI and introduced a plasmid containing TPI under the control of the inducer IPTG. The fraction of unlabeled DHAP progressively increased with IPTG addition. The extent of DHAP labeling at pseudo-steady state was used to determine the ratio of forward-to-backward TPI flux by isotopomer balancing. The flux ratio then yields ΔG as in **a**. Labeling fraction error bars represent s.d. (*n* = 3), and calculated ΔG errors represent 95% confidence intervals.
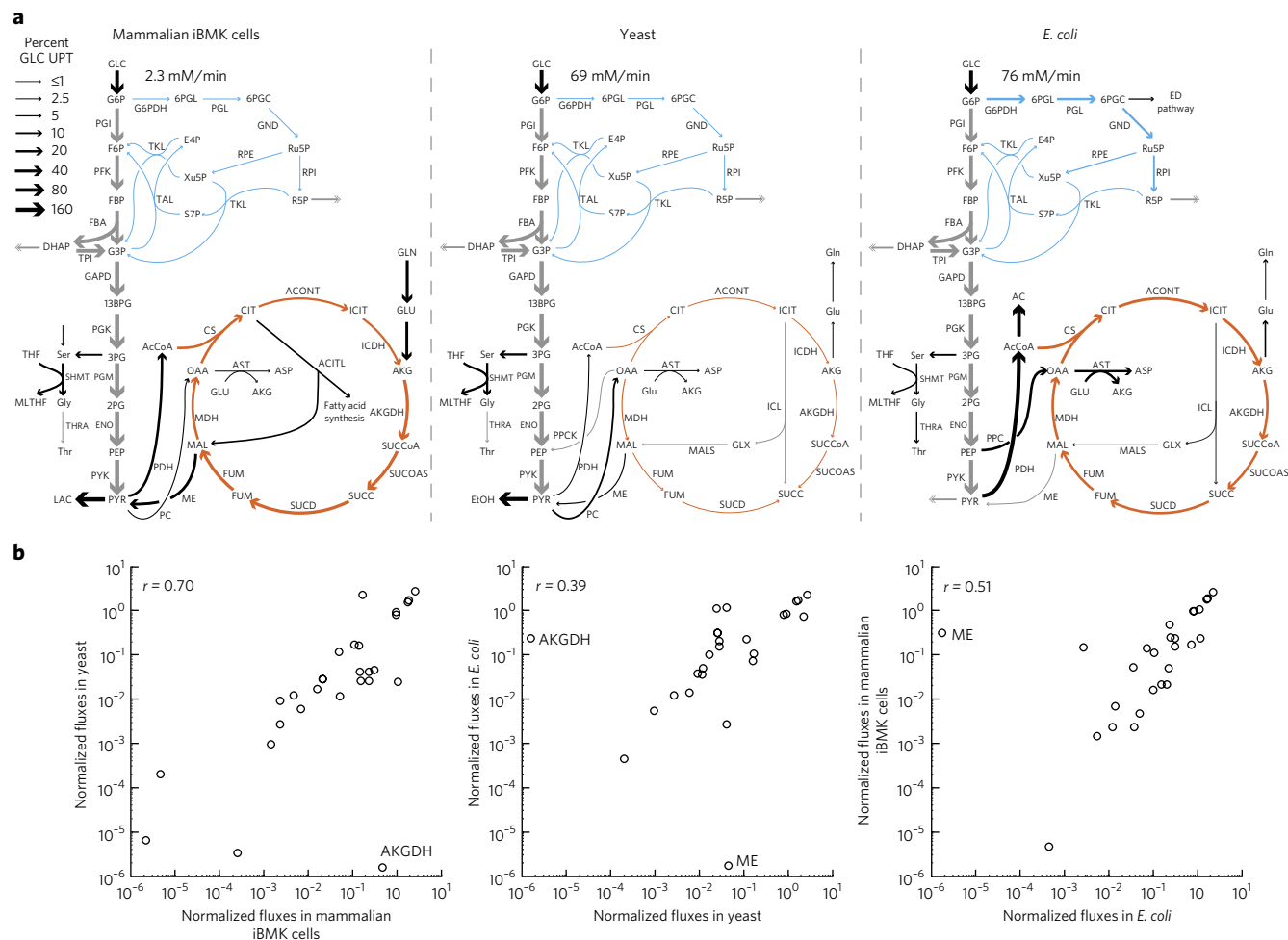
a

b

Figure 2 | Metabolic flux distributions in mammalian iBMK cells, yeast and *E. coli*. Fluxes were determined by integrating direct nutrient uptake and waste secretion rate measurements and data from multiple isotope tracers by metabolic flux analysis. (**a**) Net fluxes. Arrow widths indicate absolute magnitudes of fluxes, normalized to glucose uptake (GLC UPT), as shown in the legend. Absolute magnitude of glucose uptake is shown for each organism. Grey, glycolysis; blue, pentose phosphate pathway; orange, TCA cycle; black, other. (**b**) Comparison of normalized net fluxes across organisms. Fluxes were normalized to the organism's glucose uptake rate. Plotted data are restricted to linearly independent fluxes (for example, lower glycolysis is shown once per graph, not repeatedly for each pathway enzyme). AKGDH, α-ketoglutarate dehydrogenase; ME, malic enzyme.

unified picture of central carbon metabolite concentrations and free energies. To this end, we obtained ΔG°′ by a group contribution method (component contribution)[23] and searched for sets of central carbon metabolite concentrations that best matched both (i) the directly observed concentrations for measured metabolites and (ii) the observed cellular ΔG for measured reactions (Online Methods). For reactions in which free energy was not measured, ΔG was constrained to be negative in the direction of net flux. Metabolite sets were penalized when either concentrations or free energies fell outside of the 95% confidence intervals of the measurements. We subsequently obtained upper and lower boundaries for metabolite concentrations and reaction free energies by linear programming. This approach identified previously unmeasured absolute metabolite concentrations and more tightly constrained those of metabolites that were involved in multiple reactions with measured cellular ΔG values (for example, DHAP and pentose phosphates) (**Fig. 4a** and **Supplementary Table 3**). Notably, we were able to obtain reliable measurements for species that were difficult to measure owing to analytical interferences or instability, including ribulose-5-phosphate, erythrose-4-phosphate, 1,3-bisphosphoglycerate, 2-phosphoglycerate and oxaloacetate.

Combining these concentrations together with ΔG°′ values, we determined ΔG for most central carbon metabolic reactions (**Supplementary Table 4**). Focusing on glycolysis, the cumulative free energy change from phosphoglucose isomerase (PGI) to pyruvate kinase (PYK) was, on average, −46 kJ mol⁻¹ (**Fig. 4b**). In each case, phosphofructokinase was the most strongly forward driven glycolytic step, consuming nearly half of the available free energy. Downstream of phosphofructokinase, the available free energy was relatively evenly distributed across pathway steps except the step involving triose phosphate isomerase, which was always the reaction closest to equilibrium. Such even flux partitioning, with a bias toward fast reactions (such as the triose phosphate isomerase reaction) being close to equilibrium, has been predicted to maximize the efficiency of enzyme utilization[16].

Along with phosphofructokinase, pyruvate kinase is generally considered a committed step in glycolysis. Current textbooks indicate that almost the entire energy drop in glycolysis occurs at the phosphofructokinase and pyruvate kinase steps (**Fig. 4b**). Accordingly, we were surprised when our global analysis resulted in only a modest driving force for pyruvate kinase in the mammalian cell line iBMK (ΔG = −3.8 kJ/mol, implying a forward-to-backward flux ratio of 4.3). To evaluate further the free energy of the pyruvate kinase reaction, we added labeled pyruvate to growing cells and monitored the formation of lower glycolytic intermediates. Although the concentration of phosphoenolpyruvate was too low to measure its labeling directly, we observed labeling of 3-phosphoglycerate, confirming some back flux through the phosphoglycerate
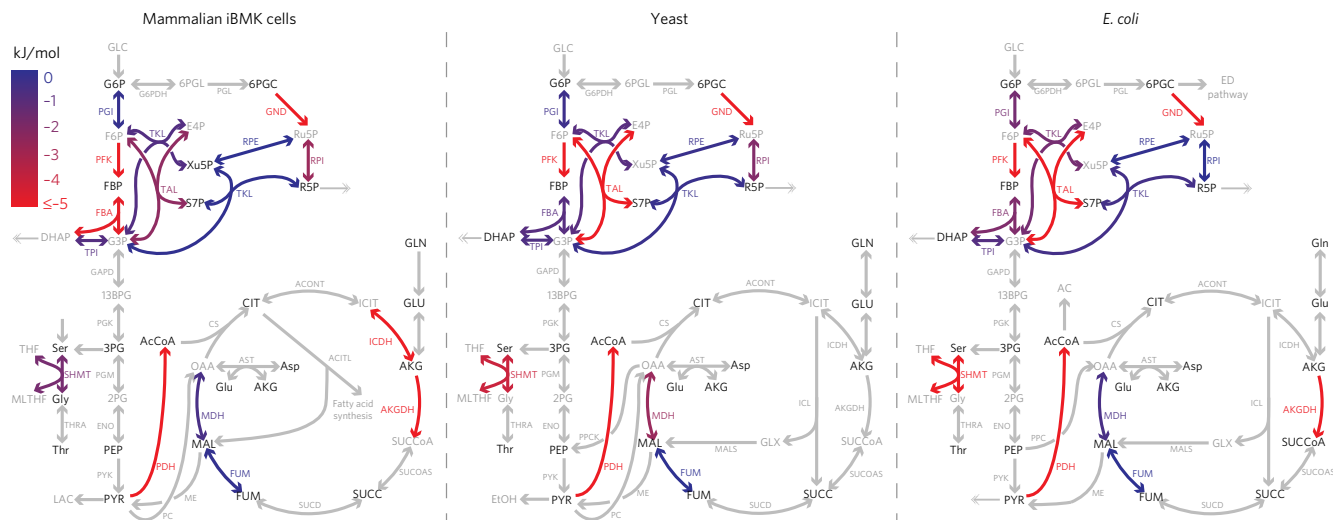
Figure 3 | Reaction free energy determined with isotope tracers in mammalian iBMK cells, yeast and *E. coli*. Flux reversibility and ΔG were determined from forward and backward fluxes. Blue, equilibrium ($\Delta G \approx 0$ kJ mol^{-1}); red, substantially forward driven ($\Delta G \leq -5$ kJ mol^{-1}); gray, not measured based solely on isotope tracer data (reversibility of glycolytic reactions inferred from combined flux and concentration data is shown in **Fig. 4b**).

mutase–enolase-pyruvate kinase reaction sequence (**Fig. 4c**). The observed labeling was not caused by canonical gluconeogenic flux, as this would have resulted in 3-phosphoglycerate being both M+2 and M+3 labeled[24], whereas only M+3 labeling was observed. Thus, the pyruvate kinase reaction can be partially reversible.

Overall, reaction free energies were highly conserved across the three organisms (**Fig. 4d**). The details of free energy utilization, however, differed. Compared to mammalian iBMK cells, yeast had higher glucose-6-phosphate, ADP/ATP and NAD$^+$/NADH, with the net effect being a near doubling of the free energy drop in glycolysis. This larger free energy drop likely facilitates rapid fermentation. Notably, despite most glycolytic reactions being more forward-driven in yeast, aldolase was closer to equilibrium. This could potentially further favor yeast fermentation by enhancing the free energy available for downstream glycolytic steps. Thus, the details of free energy partitioning may be optimized to organism-specific metabolic objectives.

Conservation of absolute metabolite concentrations

Given the fundamental connection between ΔG and metabolite concentrations, the similarity of reaction free energies across species suggested similarity in the metabolomes. A compilation of metabolite concentrations, determined by a combination of direct concentration measurements and the above approach for integrating free energy measurements, is provided in **Supplementary Table 5**. Across the organisms, amino acids comprised the largest fraction of the metabolome (**Fig. 5a**) and were similar in intracellular abundances despite the presence of amino acids in the mammalian but not the microbial culture medium. Central carbon metabolites were the next most abundant, followed by nucleotides (including nucleotide-derived cofactors such as NAD$^+$). The most abundant individual metabolite in each organism was glutamate, the amino group donor in many transamination reactions, whose high concentration may be required to drive transamination forward. Other abundant intracellular metabolites included reduced glutathione and pyruvate (**Fig. 5a**). Globally, the metabolite concentrations of *E. coli*, yeast and mammalian iBMK cells were all correlated with each other (**Fig. 5b** and **Supplementary Fig. 1**), with the fraction of variance in absolute metabolite concentrations explained by the interorganism correlation (r^2), which ranged from 40% to 70%. The remaining 30% to 60% of variance reflects some combination of measurement error and true interorganism

differences. In the previous work comparing the *E. coli* metabolome across three different carbon sources[1], we found that ~75% of variance was explained by correlation across conditions, suggesting a nutrient contribution of no more than 25%. Thus, the impact of organism on absolute metabolite concentrations is stronger than that of carbon source. Nevertheless, in spite of different lifestyles, physiology and culture conditions across organisms and the potential for metabolite concentrations to change without overt effects on cell physiology[25], absolute metabolite concentrations are substantially conserved across kingdoms of life.

Substrate and inhibitor enzyme binding site occupancy

To infer enzyme binding site occupancies, we compared the absolute concentrations of metabolites to the affinities of the enzyme sites to which they bind. Binding affinities (the inverse of the dissociation constants K_m and K_i) were taken from the BRENDA database[26] (**Supplementary Data Sets 2** and **3**). Similar prior analysis in *E. coli* had focused exclusively on substrate binding and found a propensity for most active sites to be occupied[1]. Here we validated this basic observation also for yeast and mammalian iBMK cells, with metabolite concentration exceeding K_m for roughly two-thirds of sites in each case (**Fig. 6a**). As described previously for *E. coli*, the ubiquitous cofactors ATP, NAD$^+$ and NADPH were almost always saturating. In contrast, NADP$^+$ was not reliably saturating, perhaps reflecting prioritization of a high NADPH/NADP$^+$ ratio over complete enzyme site occupancy (**Supplementary Fig. 2**). Central carbon metabolite concentrations were often near K_m, perhaps to facilitate efficient regulation or switching to gluconeogenesis[1], whereas the concentrations of the substrates of degradative enzymes (for example, of nucleotide catabolism) were typically below K_m. Such pathways are presumably useful only when substrate concentrations rise. In contrast to the general propensity for substrates to be saturating, inhibitor concentrations tended to be near or below K_i (**Fig. 6b**), despite a propensity for ATP, NAD$^+$ and NADPH to be saturating also at inhibitory sites, although to a lesser degree than at substrate ones (**Supplementary Fig. 2**). The greater propensity for substrates than inhibitors to be saturating was statistically significant in each organism (**Fig. 6c**). Thus, metabolite concentrations seem to be tuned to saturate enzyme active sites but not effector binding sites in freely growing cells. This favors efficient enzyme utilization, with inhibitor concentrations near K_i positioning the system for regulation to kick in if significant deviations from homeostasis occur.
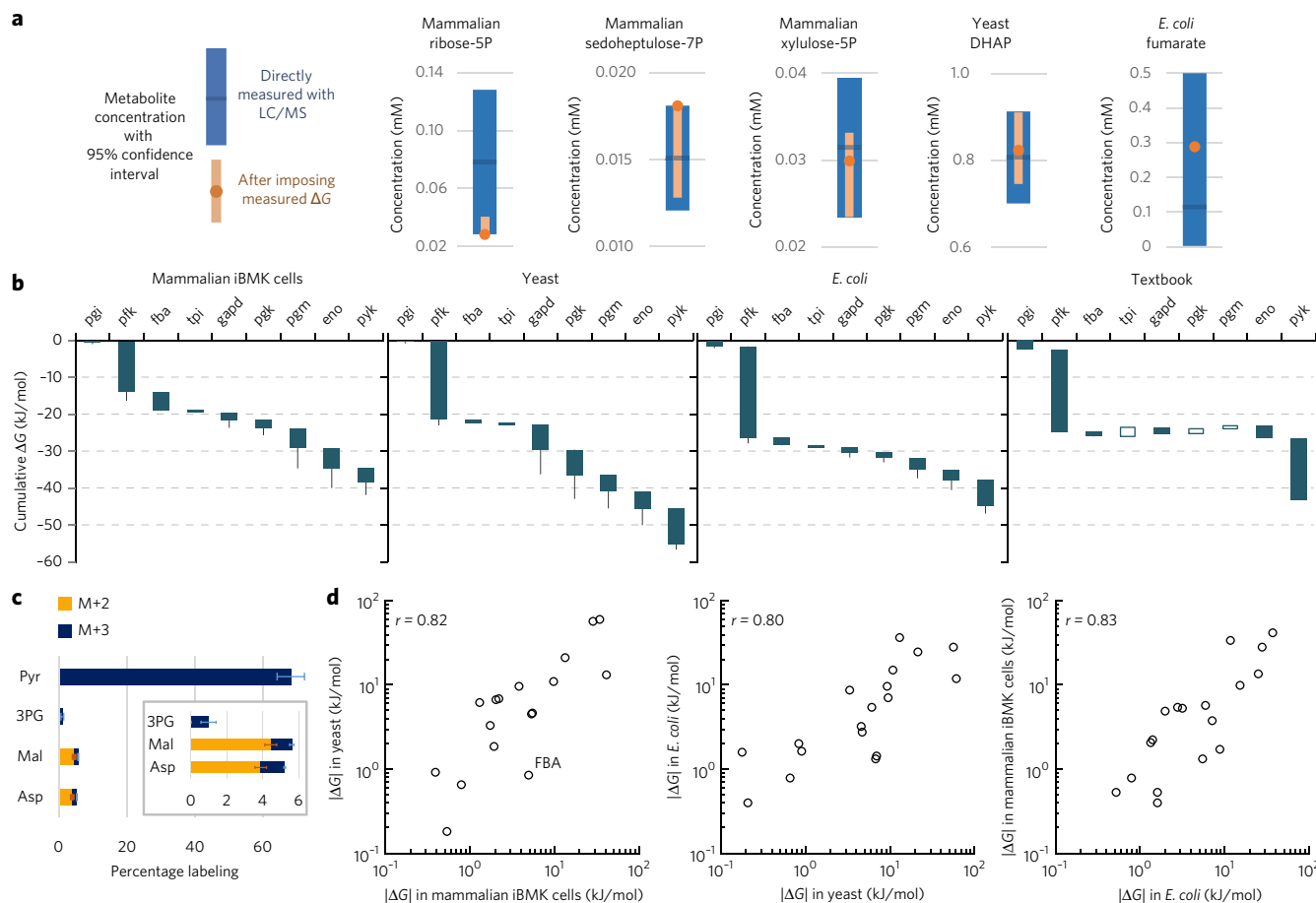
Figure 4 | Integration of flux and concentration measurements via ΔG. (**a**) The absolute concentrations of metabolites involved in reactions with ΔG determined from reaction reversibility (**Fig. 3b**) were refined by combining confidence intervals from direct LC/MS measurements of their concentrations (blue) with thermodynamic constraints to more precise obtained values (orange). For example, the concentration of fumarate is informed also by that of malate, in combination with the reversibility of fumarase. (**b**) ΔG for glycolysis based on integration of metabolite concentrations and reaction reversibilities. Blue and white bars depict negative and positive ΔG, respectively. Whiskers show 95% confidence limits (Online Methods). (**c**) An unexpected finding from the thermodynamic analysis in **b** is partial reversibility of pyruvate kinase. To directly demonstrate this reversibility, [U-^{13}C]pyruvate (0.45 mM) was added to the medium of growing iBMK cells for 20 min, and upstream and downstream metabolites were analyzed for labeling. Error bars represent s.e.m. (n = 3). Pyr, pyruvate; 3PG, 3-phosphoglycerate; Mal, malate. (**d**) Comparison of ΔG across organisms. Plotted data are for all measured reactions with ΔG < −0.1 kJ mol^{-1}.

DISCUSSION

Metabolism is the process of converting nutrient inputs into usable energy and biomass building blocks. Like all chemical networks, metabolism must obey the second law of thermodynamics: each pathway step must cost free energy. A fundamental challenge is partitioning the available free energy across pathway steps. Too large a drop in free energy at any one step wastes the energy available in scarce nutrients. Too small a drop results in the associated enzyme catalyzing unproductive backward flux.

To understand how cells manage this challenge, biochemists have long relied on the ability to infer the free energies of cellular reactions (ΔG) on the basis of metabolite concentrations combined with standard free energies[27,28], as per equation (1). Recently, such analyses have been conducted for increasingly large metabolic networks[29,30]. Here, using isotope tracers and MS, we augmented the tool set for probing cellular thermodynamics by determining relative forward-to-backward reaction fluxes and thus ΔG directly, as per equation (2). Measurement of reaction reversibility is based on the backward reaction producing a distinctive isotope labeling pattern in the substrate. This was exemplified by the formation of unlabeled DHAP via backwards triose phosphate isomerase flux after feeding [1,2-^{13}C$_2$]glucose (**Fig. 2**). To obtain forward and backward fluxes for a substantial fraction of central metabolism, we integrated data from multiple different ^{13}C tracers (**Supplementary**

Table 2). More precise and comprehensive determination of flux reversibility should be possible in the future through dynamic ^{13}C labeling experiments[31] and/or the application of ^{2}H and ^{15}N tracers as well.

Compartmentation introduces an unaccounted-for complexity into these flux and thermodynamic determinations. The analysis reported here is for metabolites collected from whole cells and does not distinguish forward-and-backward flux occurring through a single enzyme in one compartment from a pair of enzymes (such as distinct isozymes) in different compartments. Mitigating compartmentation concerns, however, similar results were obtained from *E. coli* and the eukaryotic cells, despite much more extensive compartmentation in the eukaryotes. Development of methods that enable compartmental analysis of metabolite concentrations, fluxes and free energies is an important future objective.

In addition to the methodology for measuring ΔG, a key contribution of this work is a coherent systems-level set of fluxes, free energies and metabolite concentrations for *E. coli,* yeast and the mammalian cell line iBMK (**Figs. 2–5** and **Supplementary Tables 1**, **4** and **5**). Prior work has integrated metabolite concentrations and fluxes in dynamic labeling experiments[31] on the basis of the relationship between metabolite pool sizes, turnover times and fluxes: metabolites turn over (and thus tend to label) rapidly when flux is large or pool size is small[31,32]. This relationship, which is not
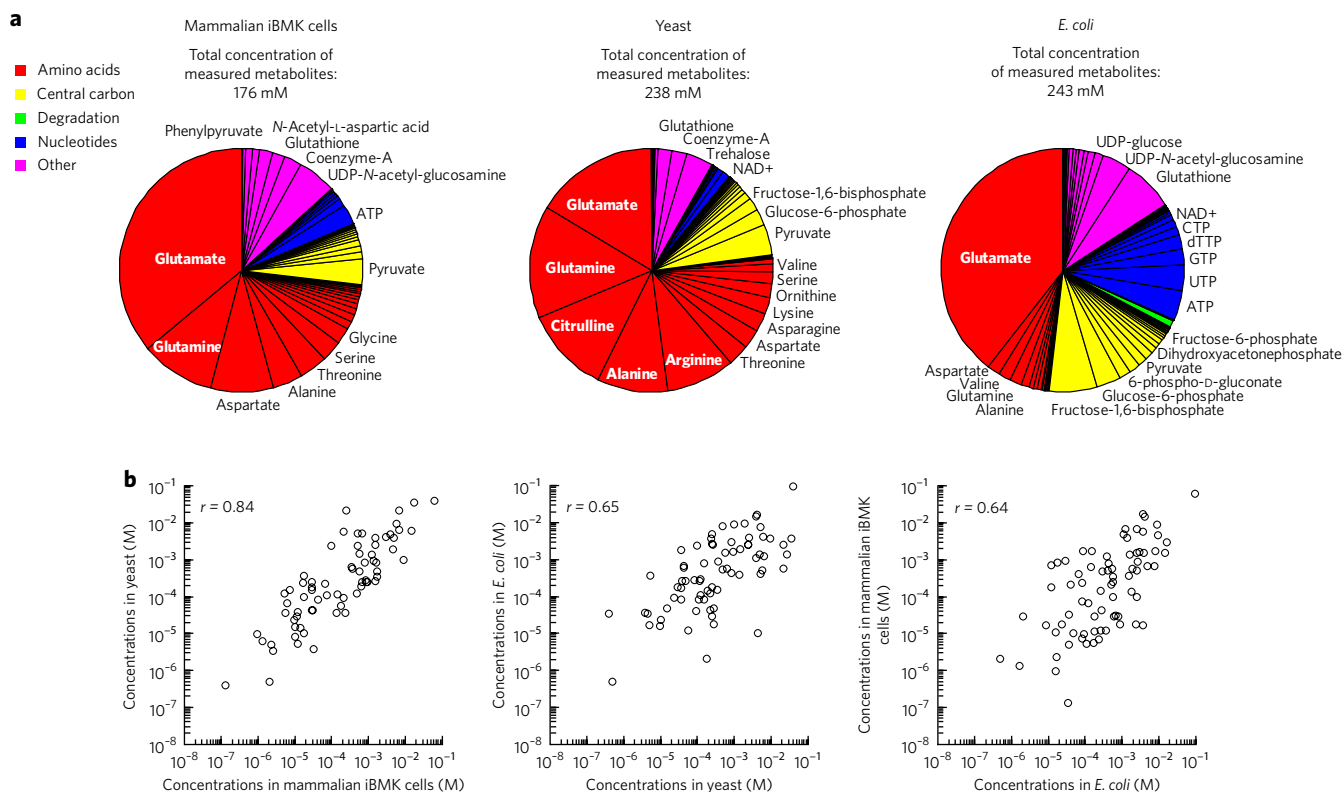
Figure 5 | Conservation of absolute metabolite concentrations. (a) Pie chart showing fractional contribution of each measured metabolite in each organism. Concentrations were obtained by the integrative analysis as in **Figure 4a**. Names are shown for metabolites whose fractional concentration exceeds 1%. **(b)** Comparison of absolute metabolite concentrations across organisms. Plotted data are for all measured metabolites.

applicable to the steady-state labeling experiments reported here, could be used to further constrain concentration and flux estimates in future work. Prior studies that are more directly related to our current approach have integrated metabolite concentration and free energies to achieve systems-level estimates of both[1,2,17]. By augmenting such thermodynamic analysis with the direct flux-based ΔG measurements for a subset of reactions, the present work markedly refines the overall thermodynamic estimates, providing useful quantitative values of cellular ΔG for many reactions.

These data shed light on metabolic design principles. Consider glycolysis, which is the highest-flux pathway in each of the studied organisms and localizes to the cytosol, obviating compartmentation concerns. The textbook view involves three strongly thermodynamically forward-driven reactions, which cannot reverse flux direction during gluconeogenesis and thus must be bypassed, linked by near-equilibrium ones that, during gluconeogenesis, flip their direction of net flux (**Fig. 4b**). The three committed reactions are glucose phosphorylation (hexokinase in yeast and in mammals and phosphotransferase system in *E. coli*), phosphofructokinase and pyruvate kinase. Glucose phosphorylation was omitted from our analysis because of our inability to quantify the intracellular glucose concentration (given the abundance of media glucose). For phosphofructokinase and pyruvate kinase, we found that the former is substantially more forward driven: ΔG for phosphofructokinase ranges from -13 kJ mol^{-1} to -25 kJ mol^{-1}, which results in minimal back flux (<0.7% of forward flux), whereas for pyruvate kinase, it ranges from approximately -4 kJ mol^{-1} to -10 kJ mol^{-1}, resulting in 2% to 20% backward-to-forward flux. Thus, although both reactions are far enough from equilibrium for changes in the associated enzyme activities to exert flux control, phosphofructokinase functions as a classic irreversible step, whereas some backward flux at pyruvate kinase is tolerated to achieve energy efficiency.

The lower free energy drop at pyruvate kinase results in a greater amount of free energy available to drive the reversible reactions of lower glycolysis. According to a standard textbook[33], the net free energy drop from fructose-1,6-bisphosphate to phosphoenolpyruvate is only 1.7 kJ mol^{-1}. Spread evenly across six reactions, this would result in a drop per reaction of only 0.3 kJ mol^{-1}, which is associated with a forward-to-backward flux ratio of roughly 10:9, or one unit of productive flux for 18 units of exchange flux, resulting in only ~5% of enzyme contributing productive net flux. Given the high cellular levels of glyceraldehyde-3-phosphate dehydrogenase, phosphoglycerate kinase and enolase[34–37], the expense of protein synthesis[38] and cellular space limitations[39], there should be strong evolutionary pressure to use these enzymes at greater than 5% efficiency. Indeed, the actual situation in cells is different from the current textbook description. The free energy drop over this six-reaction sequence is not 1.7 kJ mol^{-1} but instead at least sixfold higher (11.4–24.2 kJ mol^{-1}) (**Fig. 4b**), with only the triose phosphate isomerase step having a drop less than 2 kJ mol^{-1} in all organisms. Thus, in glucose-fed cells, the 'difficult' steps of lower glycolysis that require high enzyme levels are sufficiently forward driven to avoid excessive wasteful backwards flux.

The more even free energy distribution in lower glycolysis may affect both pathway regulation and dynamics. Unlike reactions very close to equilibrium, where changes in enzyme activities do not impact overall pathway flux, several reversible glycolytic reactions, including those involving aldolase, glyceraldehyde-3-phosphate dehydrogenase and phosphoglycerate mutase, are sufficiently forward driven, in at least some organisms, for these enzymes to exert physiologically relevant flux control. Indeed, glyceraldehyde-3-phosphate dehydrogenase is inactivated in response to oxidative stress, and this has been shown to inhibit glycolysis and thereby promote pentose phosphate pathway flux and NADPH production[40]. More generally, these observations are consistent with findings from
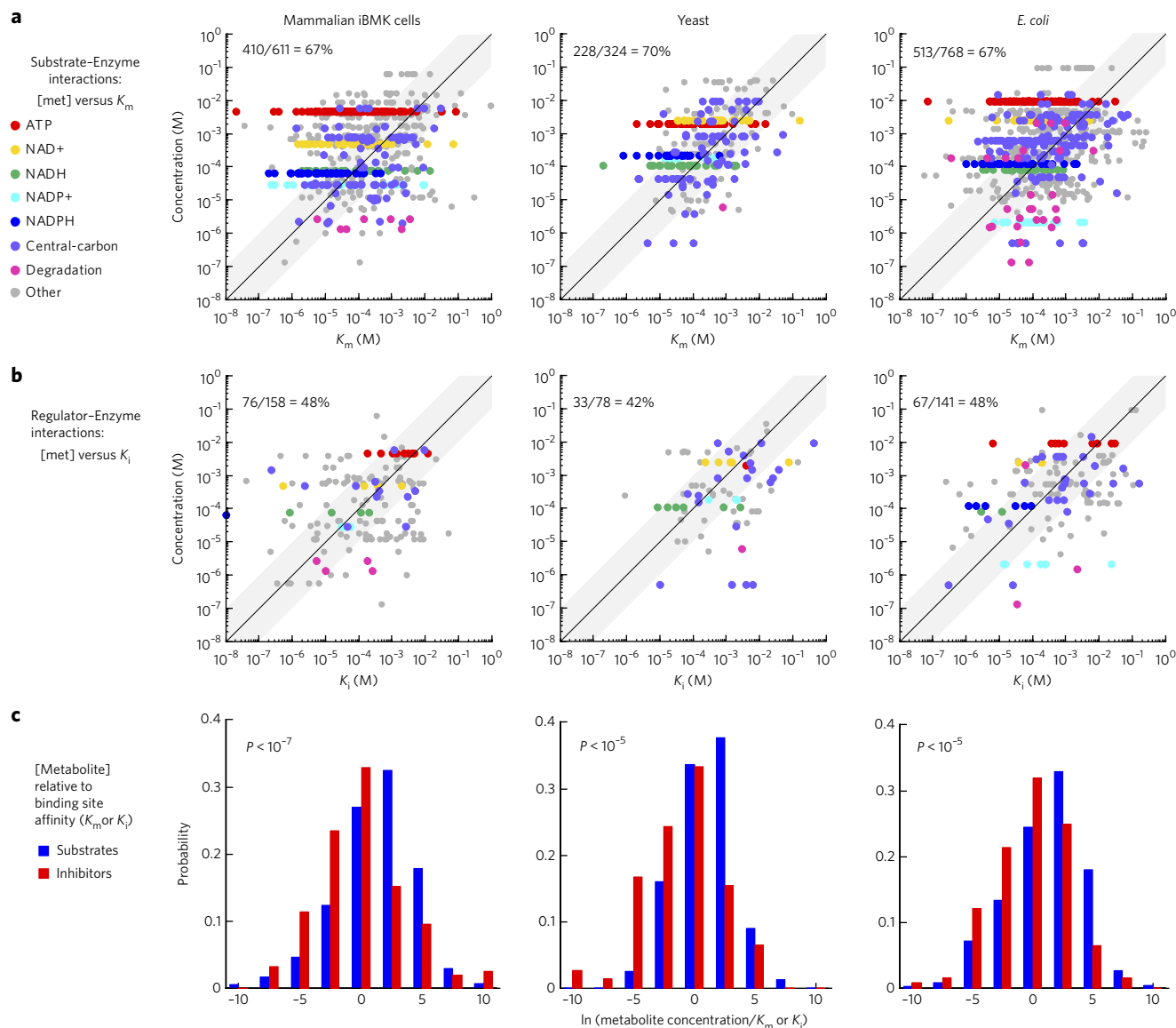
Figure 6 | Comparison of absolute concentrations to enzyme binding site affinities for substrates and for inhibitors. (**a,b**) Comparison of absolute metabolite concentrations (*y* axis) to enzyme binding site affinities (*x* axis) for binding of substrate-enzyme (**a**) and regulator-enzyme (**b**). The fraction of concentrations exceeding K_m or K_i (i.e., data points above the line of unity) is shown in the top left of each graph. (**c**) Enzyme active sites are, in general, more saturated than inhibitor sites (*P* values are from the Kolmogorov-Smirnov test).

metabolic control analysis that flux control, though unevenly distributed across glycolytic enzymes, is not concentrated in one or two key steps[41–43]. Indeed, any reaction of lower glycolysis that is substantially forward driven could be used to control pathway flux or the levels of upstream and downstream intermediates, which are themselves important precursors for biosynthetic pathways such as serine synthesis. A disadvantage of this more even free energy distribution is a slower return of the pathway intermediates to steady-state levels following perturbations and a decreased ability to control pathway flux via any single effector-enzyme interaction[44]. Apparently, at least for cells fed copious glucose, these disadvantages are outweighed by a greater efficiency of enzyme utilization, which requires a substantial driving force for all but the most rapid reactions, thereby mitigating backward flux and thus the required amount of enzyme.

Maintaining a sufficient driving force is expected to favor efficient enzyme use not only in glycolysis but also throughout metabolism. Selective pressure is presumably greatest for high-flux pathways in which adequate total free energy is available. In this respect, glycolysis in glucose-fed cells may reflect an extreme case.

Indeed, we have previously reported that lower glycolytic reactions are closer to equilibrium in cells fed glycerol (where flux remains in the glycolytic direction) or acetate (where net flow is in the opposite direction). In general, one would also expect evolutionary pressure to maintain adequate ΔG to be greatest for steps in which the total enzyme level is substantial, either due to high flux or low k_{cat}.

Throughout metabolism, substrate-to-product ratios are tied together by thermodynamics. Because each metabolite is simultaneously the substrate and product of one or more reactions, the above considerations globally constrain the concentration ratios of all metabolites. Because ΔG depends on the ratio of substrate and product concentrations, but not their absolute magnitude, other factors determine the absolute concentration of the collective metabolome. A cap on metabolite concentrations is most likely enforced by osmotics. In each of the studied organisms, the sum of all measured metabolite concentrations is around 200 mM, similar to the salt concentration in human plasma. Within this upper osmotic bound, an important determinant of absolute metabolite abundances is saturation of enzyme binding sites. Enzyme evolution is

subject to dual pressures to enhance both substrate binding affinity and turnover rate. These competing pressures are captured by the classical metric of enzyme performance, k_{cat}/K_m. Higher metabolite concentrations render low K_m values unnecessary, thereby facilitating higher k_{cat} and enabling more net flux per enzyme. Thus, there is selective pressure to maintain metabolite pools as large as feasible given thermodynamic and osmotic bounds. As for maintaining substantial thermodynamic driving force, this pressure is greatest for 'hard' reactions in high-flux pathways. Reactions may be considered hard because of universal chemical reactivity constraints or specific environmental challenges, such as nutrient scarcity. Natural variation across organisms in pathway utilization and nutrient availability should therefore result in organism-specific tailoring of absolute metabolite concentrations. The observed impressive, but incomplete, conservation of absolute metabolite concentrations reflects the balance of this tailoring against universal reactivity and thermodynamic constraints on the metabolome.

METHODS

Methods and any associated references are available in the online version of the paper.

References

1. Bennett, B.D. *et al.* Absolute metabolite concentrations and implied enzyme active site occupancy in *Escherichia coli*. *Nat. Chem. Biol.* **5**, 593–599 (2009).
2. Henry, C.S., Broadbelt, L.J. & Hatzimanikatis, V. Thermodynamics-based metabolic flux analysis. *Biophys. J.* **92**, 1792–1805 (2007).
3. Joshi, A. & Palsson, B.O. Metabolic dynamics in the human red cell. Part III—metabolic reaction rates. *J. Theor. Biol.* **142**, 41–68 (1990).
4. Chassagnole, C., Noisommit-Rizzi, N., Schmid, J.W., Mauch, K. & Reuss, M. Dynamic modeling of the central carbon metabolism of *Escherichia coli*. *Biotechnol. Bioeng.* **79**, 53–73 (2002).
5. van Eunen, K. *et al.* Measuring enzyme activities under standardized *in vivo*-like conditions for systems biology. *FEBS J.* **277**, 749–760 (2010).
6. Xu, Y.-F., Amador-Noguez, D., Reaves, M.L., Feng, X.-J. & Rabinowitz, J.D. Ultrasensitive regulation of anapleurosis via allosteric activation of PEP carboxylase. *Nat. Chem. Biol.* **8**, 562–568 (2012).
7. Cohen, P. Protein kinases—the major drug targets of the twenty-first century? *Nat. Rev. Drug Discov.* **1**, 309–315 (2002).
8. Nielsen, J. Metabolic engineering. *Appl. Microbiol. Biotechnol.* **55**, 263–283 (2001).
9. Lu, W. *et al.* Metabolomic analysis via reversed-phase ion-pairing liquid chromatography coupled to a stand alone orbitrap mass spectrometer. *Anal. Chem.* **82**, 3212–3221 (2010).
10. Büscher, J.M.,Czernik, D.,Ewald, J.C.,Sauer, U. & Zamboni, N. Cross-platform comparison of methods for quantitative metabolomics of primary metabolism. *Anal. Chem.* **81**, 3212–3221 (2004).
11. Mashego, M.R. *et al.* MIRACLE: mass isotopomer ratio analysis of U-13C-labeled extracts. A new method for accurate quantification of changes in concentrations of intracellular metabolites. *Biotechnol. Bioeng.* **85**, 620–628 (2004).
12. Bennett, B.D., Yuan, J., Kimball, E.H. & Rabinowitz, J.D. Absolute quantitation of intracellular metabolite concentrations by an isotope ratio-based approach. *Nat. Protoc.* **3**, 1299–1311 (2008).
13. Beard, D.A., Babson, E., Curtis, E. & Qian, H. Thermodynamic constraints for biochemical networks. *J. Theor. Biol.* **228**, 327–333 (2004).
14. Schellenberger, J., Lewis, N.E. & Palsson, B.Ø. Elimination of thermodynamically infeasible loops in steady-state metabolic models. *Biophys. J.* **100**, 544–553 (2011).
15. Feist, A.M. *et al.* A genome-scale metabolic reconstruction for *Escherichia coli* K-12 MG1655 that accounts for 1260 ORFs and thermodynamic information. *Mol. Syst. Biol.* **3**, 121 (2007).
16. Flamholz, A., Noor, E., Bar-Even, A., Liebermeister, W. & Milo, R. Glycolytic strategy as a tradeoff between energy yield and protein cost. *Proc. Natl. Acad. Sci. USA* **110**, 10039–10044 (2013).
17. Kümmel, A., Panke, S. & Heinemann, M. Putative regulatory sites unraveled by network-embedded thermodynamic analysis of metabolome data. *Mol. Syst. Biol.* **2**, 0034 (2006).
18. Tran, L.M., Rizk, M.L. & Liao, J.C. Ensemble modeling of metabolic networks. *Biophys. J.* **95**, 5606–5617 (2008).
19. Beard, D.A. & Qian, H. Relationship between thermodynamic driving force and one-way fluxes in reversible processes. *PLoS One* **2**, e144 (2007).
20. Wiechert, W. The thermodynamic meaning of metabolic exchange fluxes. *Biophys. J.* **93**, 2255–2264 (2007).
21. Degenhardt, K. & White, E. A mouse model system to genetically dissect the molecular mechanisms regulating tumorigenesis. *Clin. Cancer Res.* **12**, 5298–5304 (2006).
22. Xu, Y.F., Lu, W. & Rabinowitz, J.D. Avoiding misannotation of in-source fragmentation products as cellular metabolites in liquid chromatography-mass spectrometry–based metabolomics. *Anal. Chem.* **87**, 2273–2281 (2015).
23. Noor, E., Haraldsdóttir, H.S., Milo, R. & Fleming, R.M.T. Consistent estimation of Gibbs energy using component contributions. *PLoS Comput. Biol.* **9**, e1003098 (2013).
24. Katz, J., Wals, P. & Lee, W.N. Isotopomer studies of gluconeogenesis and the Krebs cycle with 13C-labeled lactate. *J. Biol. Chem.* **268**, 25509–25521 (1993).
25. Raamsdonk, L.M. *et al.* A functional genomics strategy that uses metabolome data to reveal the phenotype of silent mutations. *Nat. Biotechnol.* **19**, 45–50 (2001).
26. Schomburg, I. *et al.* BRENDA in 2013: integrated reactions, kinetic data, enzyme function data, improved disease classification: new options and contents in BRENDA. *Nucleic Acids Res.* **41**, D764–D772 (2013).
27. Minakami, S. & Yoshikawa, H. Thermodynamic considerations on erythrocyte glycolysis. *Biochem. Biophys. Res. Commun.* **18**, 345–349 (1965).
28. Vojinović, V. & von Stockar, U. Influence of uncertainties in pH, pMg, activity coefficients, metabolite concentrations, and other factors on the analysis of the thermodynamic feasibility of metabolic pathways. *Biotechnol. Bioeng.* **103**, 780–795 (2009).
29. Henry, C.S., Jankowski, M.D., Broadbelt, L.J. & Hatzimanikatis, V. Genome-scale thermodynamic analysis of *Escherichia coli* metabolism. *Biophys. J.* **90**, 1453–1461 (2006).
30. Hoppe, A., Hoffmann, S. & Holzhütter, H.G. Including metabolite concentrations into flux balance analysis: thermodynamic realizability as a constraint on flux distributions in metabolic networks. *BMC Syst. Biol.* **1**, 23 (2007).
31. Nöh, K. *et al.* Metabolic flux analysis at ultra short time scale: isotopically non-stationary 13C labeling experiments. *J. Biotechnol.* **129**, 249–267 (2007).
32. Yuan, J., Fowler, W.U., Kimball, E., Lu, W. & Rabinowitz, J.D. Kinetic flux profiling of nitrogen assimilation in *Escherichia coli*. *Nat. Chem. Biol.* **2**, 529–530 (2006).
33. Berg, J.M., Tymoczko, J.L. & Stryer, L. *Biochemistry* (W.H. Freeman, New York, 2012).
34. Liebermeister, W. *et al.* Visual account of protein investment in cellular functions. *Proc. Natl. Acad. Sci. USA* **111**, 8488–8493 (2014).
35. Valgepea, K., Adamberg, K., Seiman, A. & Vilu, R. *Escherichia coli* achieves faster growth by increasing catalytic and translation rates of proteins. *Mol. Biosyst.* **9**, 2344–2358 (2013).
36. de Godoy, L.M. *et al.* Comprehensive mass-spectrometry–based proteome quantification of haploid versus diploid yeast. *Nature* **455**, 1251–1254 (2008).
37. Geiger, T., Wehner, A., Schaab, C., Cox, J. & Mann, M. Comparative proteomic analysis of eleven common cell lines reveals ubiquitous but varying expression of most proteins. *Mol. Cell. Proteomics* **11**, 014050 (2012).
38. Dekel, E. & Alon, U. Optimality and evolutionary tuning of the expression level of a protein. *Nature* **436**, 588–592 (2005).
39. Beg, Q.K. *et al.* Intracellular crowding defines the mode and sequence of substrate uptake by *Escherichia coli* and constrains its metabolic activity. *Proc. Natl. Acad. Sci. USA* **104**, 12663–12668 (2007).
40. Ralser, M. *et al.* Dynamic rerouting of the carbohydrate flux is key to counteracting oxidative stress. *J. Biol.* **6**, 10 (2007).
41. Fell, D. *Understanding the Control of Metabolism* (Portland Press, 1997).
42. Heinrich, R. & Schuster, S. *The Regulation of Cellular Systems* (Chapman & Hall, New York, 1996).
43. Cornish-Bowden, A. *Fundamentals of Enzyme Kinetics* (Portland Press, 1995).
44. Schuster, S. & Heinrich, R. Time hierarchy in enzymatic reaction chains resulting from optimality principles. *J. Theor. Biol.* **129**, 189–209 (1987).

Author contributions

J.O.P., S.A.R., Y.-F.X., T.S. and J.D.R. designed the study. J.O.P., S.A.R., Y.-F.X., D.A.-N. and J.F. carried out the experiments. J.O.P. and S.A.R. developed the computational tools. J.O.P., S.A.R. and J.D.R. wrote the paper.

Competing financial interests

The authors declare no competing financial interests.

Additional information

Any supplementary information, chemical compound information and source data are available in the online version of the paper. Reprints and permissions information is available online at http://www.nature.com/reprints/index.html. Correspondence and requests for materials should be addressed to J.D.R.

ONLINE METHODS

Strains and culture conditions. *E. coli* K-12 strain NCM3722 was grown at 37 °C in Gutnick minimal medium[45] containing 10 mM NH_4Cl and 0.4% (w/v) D-glucose. To create the inducible triose phosphate isomerase strain, the chromosomal tpiA was knocked out by P1 phage transduction of a deletion allele with a kanamycin resistance cassette from the Keio collection, and a pAC24N::tpiA ASKA plasmid under the control of isopropyl β-D-thiogalactopyranoside (IPTG) was introduced by electroporation. *Saccharomyces cerevisiae* derived from prototrophic strains S288C and W303 were grown at 30 °C in 2% (w/v) D-glucose medium containing 6.7 g/l Difco Yeast Nitrogen Base (YNB) without amino acids. $BAX^{-/-}/BAK^{-/-}$–immortalized baby mouse kidney epithelial cells (iBMK)[21] were grown at 37 °C and 5% CO_2 in Dulbecco's modified Eagle medium without pyruvate (DMEM) supplemented with 10% dialyzed FBS. For steady-state flux analysis, *E. coli* were cultured in medium containing [1,2-$^{13}C_2$]glucose, [3-$^{13}C_1$]glucose or 50% [U-$^{13}C_6$]glucose, yeast in [1,2-$^{13}C_2$] glucose or 50% [U-$^{13}C_6$]glucose, and iBMK in [1,2-$^{13}C_2$]glucose, [U-$^{13}C_6$] glucose or [U-$^{13}C_5$]glutamine (99%, Cambridge Isotope Laboratories) until isotopic steady states were reached. Microbes were labeled starting from overnight cultures and mammalian cells were labeled for at least 24 h. To verify the reversibility of mammalian pyruvate kinase, [U-$^{13}C_3$]pyruvate (as the sodium salt) was spiked into culture medium (which had been changed 3 h beforehand) to a final concentration of 0.005% (0.45 mM), and metabolism was quenched after 20 min.

Metabolite measurements and absolute quantification. Metabolism of exponentially growing cells was quickly quenched, and metabolites were extracted in precooled extraction solvents. Briefly, small portions of *E. coli* or yeast culture (3 ml at OD_{600} ≈0.3 for *E. coli* and 0.6 for yeast) were vacuum-filtered onto nylon membrane filters (0.45 μm, Millipore) resting on a vacuum filter support. Once cells were loaded, the membranes were immediately submerged in precooled −20 °C 40:40:20 acetonitrile/methanol/water in petri dishes. For iBMK cells at ~80% confluency, cells were supplied with fresh medium, and 2–3 h thereafter the medium was aspirated, and metabolism was immediately quenched by adding −80 °C 80% methanol to the culture dishes. Extraction continued for 20 min at −20 °C, and metabolite extracts were collected into Eppendorf tubes after thoroughly washing the filters (*E. coli* and yeast) and detaching the cells from the culture plates using cell lifters (iBMK cells). The extracts were centrifuged at 4 °C. The supernatants were dried under nitrogen gas and reconstituted in HPLC-grade water for LC/MS analysis. OD_{600} (*E. coli* and *S. cerevisiae*) and packed cell volume (iBMK cells) at the time of quenching were measured and later used in calculating cellular metabolite concentrations.

For absolute metabolite quantification, cells were grown in [U-$^{13}C_6$]glucose (and also [U-$^{13}C_5$]glutamine for the mammalian cells) but otherwise the same media as above, and extraction used solvents containing known concentrations of authenticated standards[12]. *E. coli* was cultured atop filters from OD_{600} 0.03 to 0.3, with the labeled media diffusing through agarose and filters until extraction[12]. The metabolomes of *E. coli* filter culture and liquid culture are similar (**Supplementary Fig. 3**). To measure cellular concentrations of amino acids that are present in DMEM, we cultured iBMK cells in standard unlabeled DMEM and used [U-^{13}C, ^{15}N]amino acids as internal standards. In this case, cells were washed with warm PBS twice to remove exogenous amino acids before adding the extraction solvent. Nucleotides, nucleosides and bases in *E. coli* as well as NADH and NADPH in *E. coli*, yeast and mammalian cells were measured using acidic extraction solvents (0.1 M formic acid)[46]. The extracts were neutralized with 15% NH_4HCO_3 before centrifugation.

Samples were analyzed by reversed-phase ion-pairing LC coupled to a high-resolution orbitrap mass spectrometer by electrospray ionization operating in negative ion mode (Exactive, Thermo)[9,22]. Cysteine was measured after derivatization with S-methyl methanethiosulfonate (MMTS) on a LC/MS/MS instrument performing hydrophilic interaction liquid chromatography (HILIC) coupled to tandem MS in positive ion mode (Quantum Ultra, Thermo)[47]. Resulting mass spectra and chromatograms were processed using Metabolomic Analysis and Visualization Engine (MAVEN)[48] and corrected for natural ^{13}C abundance as well as incomplete labeling due to ^{12}C impurities (and also CO_2 incorporation for absolute metabolite quantification). Many LC/MS ion-specific chromatograms were complicated by multiple peaks

(for example, glucose-6-phosphate has isomers, and an ion of identical molecular formula to fumarate is produced by in-source degradation of malate). Care was taken to pick the peak at the correct retention time as validated by standard injection and not simply the largest peak of the correct exact mass. To provide additional constraints for flux analysis, some metabolite functional group labeling fractions were computed via the inverse Cauchy product of other measured metabolites (for example, the acetyl group labeling in acetyl-CoA can be computed given the labeling of both acetyl-CoA and CoA).

Uptake and secretion rate measurements. Nutrient uptake and product secretion rates were determined by the rates of disappearance and appearance of metabolites in the medium after accounting for the amount of cells and their growth rate. *E. coli* and yeast medium samples were analyzed by proton nuclear magnetic resonance (^1H-NMR) spectroscopy. To convert medium concentration changes to cellular fluxes, we used the following conversion factors: for *E. coli*, 1.0 OD_{600} = 0.47 gCDW/l, 3×10^{-13} gCDW per cell and 7×10^{-16} l aqueous volume/cell, and for yeast, 1.0 OD_{600} = 0.62 gCDW/l, 1.9×10^{-11} gCDW per cell and 5.6×10^{-14} l aqueous volume per cell[49]. For iBMK cells, the rates of glucose, glutamine and serine uptake as well as pyruvate, lactate, alanine and ammonia excretion and fatty acid biosynthesis were previously reported[50], and we assumed that 70% of packed cell volume was aqueous volume. Organism-specific biomass precursor effluxes were calculated using the measured growth rates and biomass composition incorporated in respective genome-scale models[51].

Organism-specific metabolic models. Organism-specific metabolic networks and carbon mappings were manually curated on the basis of genome-scale metabolic reconstructions[51], the BioCyc database collection (for example, HumanCyc, EcoCyc, YeastCyc) and standard textbooks. The full set of reactions included in the flux modeling is shown in **Supplementary Table 6**. Care was taken to avoid reaction inclusion bias by considering all known routes to and from experimentally measureable metabolites and their neighboring compounds in the networks. Reactions and metabolites included in the networks were mapped to their corresponding identification numbers in the Kyoto Encyclopedia of Genes and Genomes (KEGG)[52], BRaunschweig ENzyme DAtabase (BRENDA)[26] and a Biochemical Genetic and Genomic Knowledgebase (BiGG)[51] to facilitate integration among these databases.

Metabolic flux analysis including determination of flux ratios with confidence intervals. Using the carbon mapping networks and 13CFLUX2 (http://www.13cflux.net/) package[53], we obtained cumulated isotopomer models[54] for further analysis in MATLAB (MathWorks). Under net flux balance constraint, optimal balanced flux distributions (a vector with two entries per reaction, one for the net flux and another for exchange flux, the exchange flux was constrained to be negligible for known strongly thermodynamically forward-driven reactions) were obtained by minimizing the variance-weighted sum of squared residuals between the simulated and experimental (i) isotope distributions and (ii) uptake and excretion rates using the interior-point algorithm:

$$\min_{v} \sum \left(\frac{iso_{exp} - iso(v)}{s_{iso}} \right)^2 + \sum \left(\frac{v_{exp} - v}{s_v} \right)^2$$

v is flux, $iso(v)$ is simulated labeling, and s is the measurement standard deviation. Each flux distribution simulated all isotope tracer studies simultaneously for individual organisms. To account for other potential local minima, the non-convex optimization problem was solved starting from over a thousand initial flux sets until similar flux sets that best simulated the experimental data were obtained repeatedly.

To determine confidence intervals, (i) the net and the exchange flux for each reaction were each, one-by-one, successively increased or decreased, (ii) the other fluxes were again optimized with one flux fixed, (iii) any balanced flux sets where the variance-weighted sum of squared residuals did not increase by more than a fixed value (χ^2) were accepted[55] and (iv) for those accepted flux sets, forward fluxes, backward fluxes and their ratios for all reactions were calculated from the resulting net and exchange fluxes. To obtain 95% confidence intervals, the χ^2 cutoff (1 degree of freedom) was 3.84. Maximum and minimum values (among the accepted flux distributions) of each individual

flux and of the forward-to-backward flux ratios are reported as the 95% confidence intervals. The algorithm was scripted in MATLAB to run in parallel on Linux clusters and is available as open-source code at https://github.com/PrincetonUniversity/flux-ratio-based-gibbs-energy.

Standard Gibbs free energy. Component contribution[23] was performed in MATLAB to calculate standard Gibbs free energy of formation ($\Delta_f G^{o\prime}$) and reaction ($\Delta G^{o\prime}$) at physiological ionic strength, pH and electric potential. According to extended Debye-Hückel theory, determination of $\Delta G^{o\prime}$ at physiological ionic strength serves to incorporate the activity coefficients of reactants and products into $\Delta G^{o\prime}$, thereby allowing calculation of Q on the basis of concentrations, not activities. For example, component contribution takes into account the effect of [Mg^{2+}] on the $\Delta G^{o\prime}$ of ATP hydrolysis by using the data from the NIST Thermodynamics of Enzyme-Catalyzed Reactions database regarding the ATP hydrolysis equilibrium constant at typical cellular Mg^{2+} concentration. Compartment-specific values for ionic strength, pH and electric potential were employed, where 'c' stands for cytosol, 'e' for extraorganism, 'p' for periplasm and 'm' for mitochondria: for *E. coli*[15], compartment = ['c', 'e', 'p'], pH = [7.7, 7.2, 7.2], ionic strength (M) = [0.25, 0.25, 0.25], electric potential relative to cytosol (mV) = [0, 90, 90][56]; for yeast, compartment = ['c', 'e', 'm'], pH = [7.2, 5.4, 7.5], ionic strength (M) = [0.14, 0.14, 0.14], electric potential relative to cytosol (mV) = [0, 128, −155][5]; and for iBMK cells, compartment = ['c', 'e', 'm'], pH = [7.2, 7.4, 8.0], ionic strength (M) = [0.15, 0.15, 0.15], electric potential relative to cytosol (mV) = [0, 30, −155][57]. The sensitivity of $\Delta G^{o\prime}$ on pH and ionic strength and the standard error of $\Delta G^{o\prime}$ are shown in **Supplementary Tables 7** and **8**. The uncertainties were generally greater than the perturbations of $\Delta G^{o\prime}$ resulting from changes up to ± 0.4 pH and ± 0.1 M ionic strength, and therefore, the impact of pH and ionic strength variation within these ranges should minimally affect the subsequent integrative analysis.

Integration of metabolite concentrations and Gibbs free energies. The set of metabolite concentrations ([met]) and reaction free energies (ΔG) associated with central carbon metabolism (CCM; **Supplementary Fig. 4**) that best matched (i) the directly observed concentrations for measured metabolites ([met]$_{exp}$) and (ii) the observed cellular ΔG for measured reactions (ΔG_{exp}) were computed. An important consideration in this calculation is that literature values for $\Delta G^{o\prime}$ may themselves contain error. In addition, these $\Delta G^{o\prime}$ values are interrelated, such that $\Delta G^{o\prime}$ for any sequence of metabolic reactions must be given by the sum of the formation energies of the products minus the formation energies of the reactants. Accordingly, we set out to optimize both metabolite concentrations and formation energies so as to maximize consistency with prior estimates of $\Delta_f G^{o\prime}$ on the basis of the component contribution method (which itself incorporates prior literature data on $\Delta G^{o\prime}$) and our experimental observations of metabolite concentrations and cellular reaction free energies. To this end, a quadratic programming problem was formulated with independent variables ln[met] and $\Delta_f G^{o\prime}$, with the optimization objective of minimizing the departure from the expected $\Delta_f G^{o\prime}$ and measured ln[met] and ΔG:

$$\min_{\ln[\text{met}],\Delta_f G^{o\prime} \in \text{CCM}} \frac{1}{N_{exp}^{met}}\sum\left(\frac{\ln[\text{met}]_{exp}-\ln[\text{met}]}{S_{met}}\right)^2 + \frac{1}{N_{exp}^{for}}\sum\left(\frac{\Delta_f G^{o\prime}_{exp}-\Delta_f G^{o\prime}}{s_{\Delta_f G}}\right)^2$$
$$+ \frac{1}{N_{exp}^{rxn}}\sum\left(\frac{\Delta G_{exp}-\Delta G}{S_{\Delta G}}\right)^2$$

where $\overrightarrow{\Delta G} = S^T(\overrightarrow{\Delta_f G}^{o\prime} + RT\overrightarrow{\ln[\text{met}]})$,

subject to $\ln[\text{met}] \in [\ln[\text{met}]_{exp} - 2s_{met}, \ln[\text{met}]_{exp} + 2S_{met}]$,

$$\Delta_f G^{o\prime} \in [\Delta_f G^{o\prime}_{exp} - 2S_{\Delta_f G}, \Delta_f G^{o\prime}_{exp} + 2S_{\Delta_f G}]$$

and $\Delta G \in [\Delta G_{exp} - 2S_{\Delta G}, \Delta G_{exp} + 2S_{\Delta G}]$

S is the stoichiometric matrix with rows and columns representing individual metabolites and reactions, respectively. $\overrightarrow{\Delta G} = (\overrightarrow{\Delta_f G}^{o\prime}$ and $\overrightarrow{\ln[\text{met}]})$ are vectors of free energy of reaction, standard free energy of formation and log concentrations.

s refers to the standard errors of the measurements or component contribution estimates, respectively. N_{exp}^{for}, N_{exp}^{met} and N_{exp}^{rxn} are the number of input metabolite formation energies, experimentally measured metabolite concentrations and ΔG, respectively.

For reactions whose ΔG values were not precisely determined, ΔG was constrained to be negative in the direction of net flux. For the eukaryotic cells, $\Delta_f G^{o\prime}$ of TCA metabolites depended on whether they are in cytosol or mitochondria owing to pH difference across compartments, and the values of $\Delta_f G^{o\prime}$ calculated for mitochondria were used. Inorganic phosphate concentrations were input as follows: 20 mM in *E. coli*[58], 50 mM in yeast[5] and 5 mM in mammalian iBMK cells[59]. Mitochondrial coenzyme A concentration was input as 5 mM[60]. The inorganic phosphate and coenzyme A concentrations were allowed to vary within 20% of these values.

Confidence intervals of metabolite concentrations and reaction free energies. The lower and upper bounds for individual metabolite concentrations were determined by searching within the experimentally measured metabolite concentration 95% confidence interval for the minimum and maximum concentrations that also resulted in ΔG falling within its measured 95% confidence interval. Because ΔG is linear with respect to ln[met], concentration lower bounds were obtained by solving the following linear programming problem[17]:

$$\min_{\ln[\text{met}]\in \text{CCM}} \ln[\text{met}],$$

subject to $\ln[\text{met}] \in [\ln[\text{met}]_{exp} - 2s_{met}, \ln[\text{met}]_{exp} + 2s_{met}]$,

and $\Delta G \in [\Delta G_{exp} - 2s_{\Delta G}, \Delta G_{exp} + 2s_{\Delta G}]$,

where $\overrightarrow{\Delta G} = S^T(\overrightarrow{\Delta_f G}^{o\prime} + RT\overrightarrow{\ln[\text{met}]})$

For upper bound calculation, $\max_{\ln[\text{met}]\in \text{CCM}} \ln[\text{met}]$ was solved with the same set of constraints.

Similarly, reaction free energy lower bounds were obtained by solving:

$$\min_{\ln[\text{met}]\in \text{CCM}} \Delta G,$$

where $\overrightarrow{\Delta G} = S^T(\overrightarrow{\Delta_f G}^{o\prime} + RT\overrightarrow{\ln[\text{met}]})$,

subject to $\ln[\text{met}] \in [\ln[\text{met}]_{exp} - 2s_{met}, \ln[\text{met}]_{exp} + 2s_{met}]$,

and $\Delta G \in [\Delta G_{exp} - 2s_{\Delta G}, \Delta G_{exp} + 2s_{\Delta G}]$

For upper bound calculation, $\max_{\ln[\text{met}]\in \text{CCM}} \Delta G$ was solved with the same set of constraints. The linear programming problem was solved using MATLAB linprog function (interior point algorithm).

Michaelis and inhibitor dissociation constants, K_m and K_i. The Python implementation of the Simple Object Access Protocol (SOAPpy) was employed to extract the K_m and K_i values in *E. coli*, *S. cerevisiae*, *Mus musculus* and *Homo sapiens* from BRENDA[26]. The exported data were further processed to remove entries for mutant enzymes. The parameters for mammalian cells are from enzymes in *M. musculus* whenever possible but otherwise are from *Homo sapiens*. When multiple entries for the same enzyme-metabolite pair were available, its K_m or K_i was represented by their geometric mean.

Code availability. The code used for flux and flux ratio calculation, metabolite concentration and Gibbs energy integration, confidence interval determination, the SOAPpy script, the carbon mapping and cumulated isotopomer models are available on the GitHub public repository: https://github.com/PrincetonUniversity/flux-ratio-based-gibbs-energy.

45. Gutnick, D., Calvo, J.M., Klopotow, T. & Ames, B.N. Compounds which serve as sole source of carbon or nitrogen for *Salmonella typhimurium* Lt-2. *J. Bacteriol* **100**, 215 (1969).
46. Rabinowitz, J.D. & Kimball, E. Acidic acetonitrile for cellular metabolome extraction from *Escherichia coli*. *Anal. Chem.* **79**, 6167–6173 (2007).

47. Bajad, S.U. *et al.* Separation and quantitation of water soluble cellular metabolites by hydrophilic interaction chromatography-tandem mass spectrometry. *J. Chromatogr. A* **1125**, 76–88 (2006).

48. Clasquin, M.F., Melamud, E. & Rabinowitz, J.D. LC/MS data processing with MAVEN: a metabolomic analysis and visualization engine. *Curr. Protoc. Bioinformatics* **37**, 14.11.1–14.1.23 (2012).

49. Sundararaj, S. *et al.* The CyberCell Database (CCDB): a comprehensive, self-updating, relational database to coordinate and facilitate in silico modeling of *Escherichia coli*. *Nucleic Acids Res.* **32**, D293–D295 (2004).

50. Fan, J. *et al.* Glutamine-driven oxidative phosphorylation is a major ATP source in transformed mammalian cells in both normoxia and hypoxia. *Mol. Syst. Biol.* **9**, 712 (2013).

51. Schellenberger, J., Park, J.O., Conrad, T.M. & Palsson, B.Ø. BiGG: a biochemical genetic and genomic knowledgebase of large scale metabolic reconstructions. *BMC Bioinformatics* **11**, 213 (2010).

52. Kanehisa, M. *et al.* Data, information, knowledge and principle: back to metabolism in KEGG. *Nucleic Acids Res.* **42**, D199–D205 (2014).

53. Weitzel, M. *et al.* 13CFLUX2--high-performance software suite for 13C-metabolic flux analysis. *Bioinformatics* **29**, 143–145 (2013).

54. Wiechert, W., Möllney, M., Isermann, N., Wurzel, M. & de Graaf, A.A. Bidirectional reaction steps in metabolic networks: III. Explicit solution and analysis of isotopomer labeling systems. *Biotechnol. Bioeng.* **66**, 69–85 (1999).

55. Antoniewicz, M.R., Kelleher, J.K. & Stephanopoulos, G. Determination of confidence intervals of metabolic fluxes estimated from stable isotope measurements. *Metab. Eng.* **8**, 324–337 (2006).

56. Fleming, R.M.T., Thiele, I. & Nasheuer, H.P. Quantitative assignment of reaction directionality in constraint-based models of metabolism: application to *Escherichia coli*. *Biophys. Chem.* **145**, 47–56 (2009).

57. Haraldsdóttir, H.S., Thiele, I. & Fleming, R.M.T. Quantitative assignment of reaction directionality in a multicompartment human metabolic reconstruction. *Biophys. J.* **102**, 1703–1711 (2012).

58. Rosenberg, H., Russell, L.M., Jacomb, P.A. & Chegwidden, K. Phosphate exchange in the pit transport system in *Escherichia coli*. *J. Bacteriol.* **149**, 123–130 (1982).

59. Traut, T.W. Physiological concentrations of purines and pyrimidines. *Mol. Cell. Biochem.* **140**, 1–22 (1994).

60. Leonardi, R., Zhang, Y.M., Rock, C.O. & Jackowski, S. Coenzyme A: back in action. *Prog. Lipid Res.* **44**, 125–153 (2005).